



Article

Dynamic Performance Enhancement of a Direct-Driven PMSG-Based Wind Turbine Using a 12-Sectors DTC

Abdullah Eial Awwad

Department of Electrical Power Engineering and Mechatronics, Faculty of Engineering, Tafila Technical University, Tafila 66110, Jordan; abdullah.awad@ttu.edu.jo

Abstract: This paper focuses on the performance analysis, modeling, and control of permanent magnet synchronous generator (PMSG)-based wind energy conversion. This work analyzes controllers for the machine-side converter (MSC) and grid-side converter (GSC) and presents a new direct torque control (DTC) scheme based on a 12-sectors polygonal DTC for variable speed control of the PMSG. The proposed method solves the drawbacks faced by conventional six-sectors DTC control. The proposed method utilizes 12 sectors of 30° each compared to 60° in the conventional 6-sectors DTC. The 12-sectors technique was applied to voltages and flux vectors to increase the degrees of freedom for the selection of optimal vectors and, thus, reduce the torque ripple. This work analyzed the aforementioned DTC methods using MATLAB/Simulink, comparing the dynamic response of the proposed 12-sectors DTC with the conventional 6-sectors DTC control, and the results verified the effectiveness of the proposed DTC control.

Keywords: direct torque control (DTC); flux ripple; permanent magnet synchronous generator (PMSG); torque ripple; twelve-sector methodology; wind energy conversion system (WECS); wind turbine; LCL filter



Citation: Eial Awwad, A. Dynamic Performance Enhancement of a Direct-Driven PMSG-Based Wind Turbine Using a 12-Sectors DTC. *World Electr. Veh. J.* **2022**, *13*, 123. <https://doi.org/10.3390/wevj13070123>

Academic Editors: Syed Sabir Hussain Bukhari, Jorge Rodas, Jesús Doval-Gandoy and Joeri Van Mierlo

Received: 15 May 2022

Accepted: 30 June 2022

Published: 4 July 2022

Publisher's Note: MDPI stays neutral with regard to jurisdictional claims in published maps and institutional affiliations.



Copyright: © 2022 by the author. Licensee MDPI, Basel, Switzerland. This article is an open access article distributed under the terms and conditions of the Creative Commons Attribution (CC BY) license (<https://creativecommons.org/licenses/by/4.0/>).

1. Introduction

With the global climate problem becoming increasingly prominent, the demand for renewable energy resources is rising. Due to having lower operating costs than other green energy sources, wind energy is considered the most promising form of renewable energy [1].

The double-fed induction generator (DFIG) and the direct-drive permanent magnet synchronous generator (PMSG) are widely used for variable speed wind energy conversion systems (VS-WECS). The PMSG has many advantages and is considered a significant competitor to DFIG. The absence of a gearbox and its full decoupling from the grid, high power density, and easy control mechanism are the main benefits of using the PMSG in VS-WECS [1,2].

The PMSG is connected to the grid by means of a grid-side converter (GSC) and a machine-side converter (MSC). In terms of the control, different control techniques for PMSG-based wind power have been discussed in the literature. Direct torque control (DTC) and field-oriented control (FOC) are the most popular control strategies used in VS-WECS. These two control strategies have been studied and analyzed in previous research [3–5], which compared the performance of DTC and FOC based on the space vector modulation (SVM) technique. Prior work introduced an optimized DTC-PWM with constant switching frequency and a dead-time compensation [6].

Furthermore, a previous study introduced a simplified model predictive-DTC (MP-DTC) for PMSG [7], which significantly minimizes the computational effort [8,9]. Moreover, different types of sliding-mode control (SMC) applied to VS-WECS, such as second-order SMC, fuzzy SMC (F-SMC), and integral SMC (I-SMC), have previously been discussed [10–13]. The results were compared with conventional control strategies and indicated good control effects of the SMCs.

Reference [14] proposed a control strategy for the PMSG wind energy generation system based on vector control theory (VC) for the MSC and GSC. The results showed a good dynamic and steady-state performance. A new control for a grid-connected PMSG-based wind turbine structure was introduced in [15] by using the predictive controllers and state estimators. However, this method needs more parameter tuning efforts. The authors of [16] proposed a new adaptive perturb and observe (AD-PO) and hybrid P&O (HB-PO) for a grid-connected PMSG. A fast-tracking speed with low ripples was achieved using this strategy.

Another previous study proposed a direct power control (DPC) based on SMC for the grid-connected WECS [17] in which the active and reactive power compensation components were simply calculated without engaging the decomposition of positive-sequence voltage and negative-sequence stator current.

Another study proposed a new robust variable-step perturb-and-observe (RVS-P&O)-based MPPT algorithm [18]. The proposed approach was applied to a wind-turbine-based PMSG. The results showed the superiority of the robust variable-step P&O over the competing-based P&O techniques.

This paper focused on the performance analysis, modeling, and control of a PMSG-based WECS, introduced a mathematical model of the complete WECS, and analyzed the MSC and GSC controllers. The six-sectors DTC was applied to the MSC, and some drawbacks that affect system reliability and performance were noticeable, such as high ripples in the electromagnetic torque, current, and flux. To overcome this problem, a 12-sectors DTC control was proposed. This work used a DTC with 12 sectors of 30° each compared to 60° in the conventional 6-sectors DTC and, thus, the switching became more accurate. The proposed controller was verified on a PMSG-based VS-WECS. The simulations were carried out in the MATLAB/Simulink environment, and the characteristics of the PMSG for two different DTC algorithms are discussed and compared to satisfy the best topology in relation to torque, flux ripple calculations, and the spectrum analysis of the stator current.

2. WECS System Modeling

The system configuration of the PMSG-based WECS is presented in Figure 1. The system consisted of a direct-driven PMSG connected to the grid through a back-to-back (BTB) power converter. The BTB power converter had two converters, an MSC, which was designed to achieve the maximum power point tracking (MPPT), and a GSC, which was designed to stabilize the direct current (DC) link voltage at the rated value and control the reactive power.

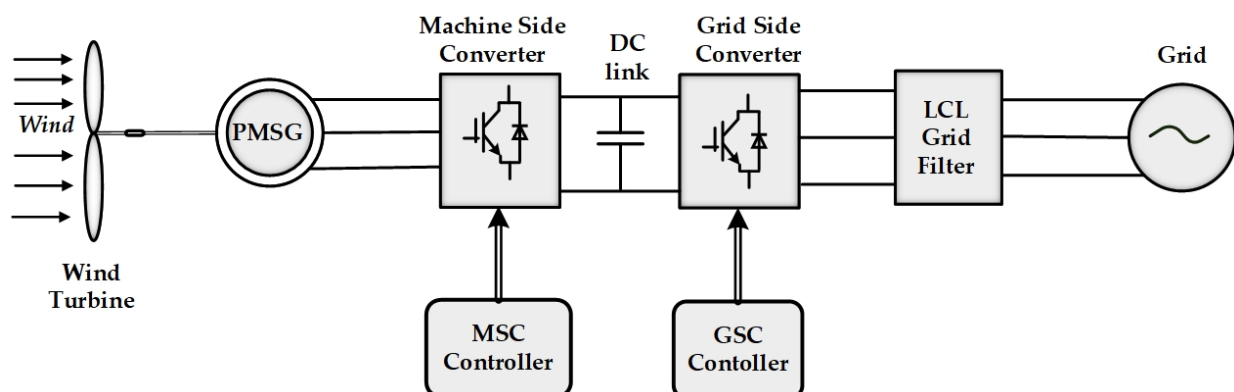


Figure 1. Configuration of a gearless PMSG-based WECS connected to a grid through a BTB power converter.

2.1. Mechanical Model of a Wind Turbine

The aerodynamic mechanical power (P_m) as a function of the effective wind speed (v) can be described as follows [19,20]:

$$P_m = \frac{1}{2} \pi \rho C_p(\lambda, \beta) r^2 v^3 \tag{1}$$

where ρ is the air density (1.225 kg/m^3); C_p is the coefficient of power conversion; r is the blade tip radius (m); λ is the tip speed ratio (TSR); β is the blade pitch angle in degrees.

The coefficient C_p is a function of (λ, β) and can be expressed as follows [20]:

$$C_p(\lambda, \beta) = c_1 \left[\frac{c_2}{\lambda_i} - c_3 \beta - c_4 \right] e^{-\left(\frac{c_5}{\lambda_i}\right)} + c_6 \lambda \tag{2}$$

$$\begin{cases} \lambda_i = \frac{1}{\lambda + 0.08\beta} - \frac{0.035}{\beta^3 + 1} \\ \lambda = \frac{r\omega_m}{v} \\ \omega_m = \omega_t G_r \end{cases} \tag{3}$$

where ω_m is the mechanical rotational speed of the PMSG; ω_t is the turbine rotational speed; G_r is the gear ratio ($G_r = 1$, gearless PMSG); the coefficients c_1 to c_6 [20] are $c_1 = 0.5176$; $c_2 = 116$; $c_3 = 0.4$; $c_4 = 5$; $c_5 = 21$; $c_6 = 0.0068$.

Assuming a single mass model of the drive train system, the mechanical equation of the wind turbine can be defined as follows:

$$T_m = J_{eq} \frac{d\omega_m}{dt} + B\omega_m + T_e \tag{4}$$

where T_m is the turbine-driving torque (N·m); J_{eq} is the total equivalent inertia of the turbine and generator ($\text{kg}\cdot\text{m}^2$); B is the damping coefficient representing the turbine and generator rotational losses ($\text{N}\cdot\text{m}\cdot\text{s}$); T_e is the electromagnetic torque of the generator (N·m).

The complete block diagram of the dynamic model of the wind turbine is summarized in Figure 2.

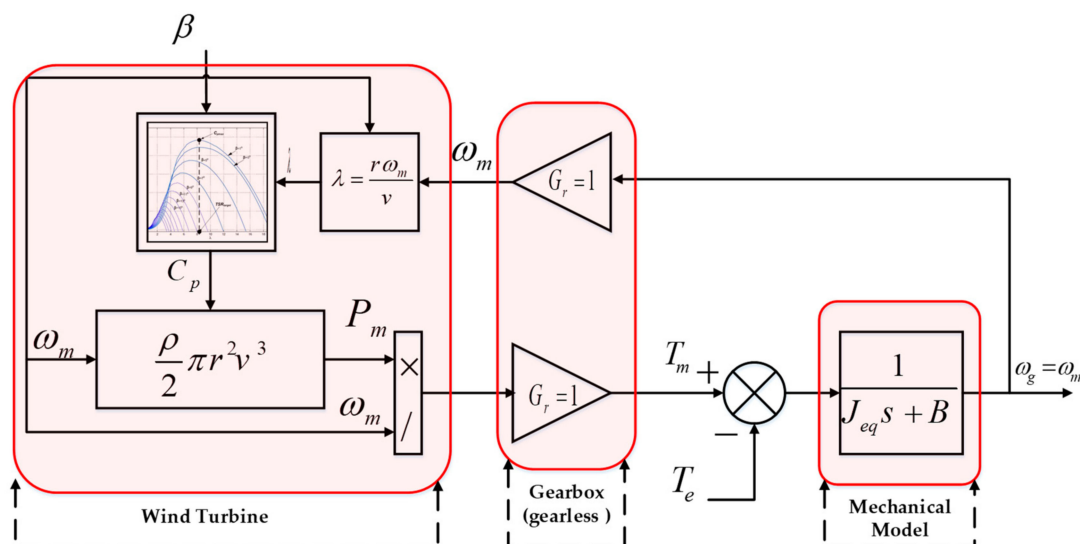


Figure 2. Dynamic block diagram of the wind turbine.

2.2. PMSG Modeling

The dynamic model of the PMSG has been reviewed in previous research [21–23]. The equivalent circuit of PMSG in the d - q axis reference frame is shown in Figure 3. Based on

that, the dynamic voltage equations, v_q and v_d , expressed in the d - q frame can be written as follows:

$$v_q = Ri_q + L_q \frac{di_q}{dt} + \omega_e(L_d i_d + \varphi_f) \tag{5}$$

$$v_d = Ri_d + L_d \frac{di_d}{dt} - \omega_e L_q i_q \tag{6}$$

where, v_q , v_d , i_q , and i_d are the d - q axis components of the stator voltages and currents, respectively; R is the stator resistance; L_q and L_d are the d - q axis inductance; φ_f is the permanent flux linkage; ω_e is the electrical rotating speed of the generator. In addition, the electromagnetic torque can be expressed as follows:

$$T_e = \frac{3P}{2} \left((L_d - L_q) i_d i_q + \varphi_f i_q \right) \tag{7}$$

where P is the number of pole pairs.

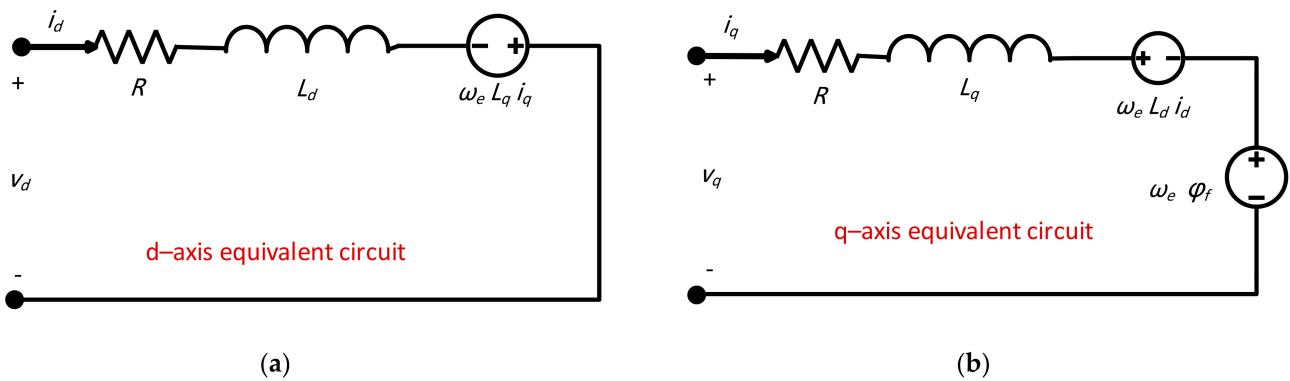


Figure 3. Equivalent dynamic model of PMSG in (a) d -axis and (b) q -axis.

The final dynamic model of the PMSG in the d - q reference frame can be expressed as follows:

$$\begin{cases} \frac{di_q}{dt} = -\frac{R}{L_q} i_q - \frac{L_d}{L_q} \omega_e i_d - \frac{1}{L_q} \omega_e \varphi_f + \frac{1}{L_q} v_q \\ \frac{di_d}{dt} = -\frac{R}{L_d} i_d + \frac{L_q}{L_d} \omega_e i_q + \frac{1}{L_d} v_d \\ T_e = \frac{3P}{2} \left((L_d - L_q) i_d i_q + \varphi_f i_q \right) \\ \frac{d\omega_m}{dt} = \frac{1}{J_{eq}} T_m - \frac{1}{J_{eq}} T_e - \frac{B}{J_{eq}} \omega_m \end{cases} \tag{8}$$

According to Equation (8), the block diagram of the dynamic model of the PMSG was derived as shown in Figure 4.

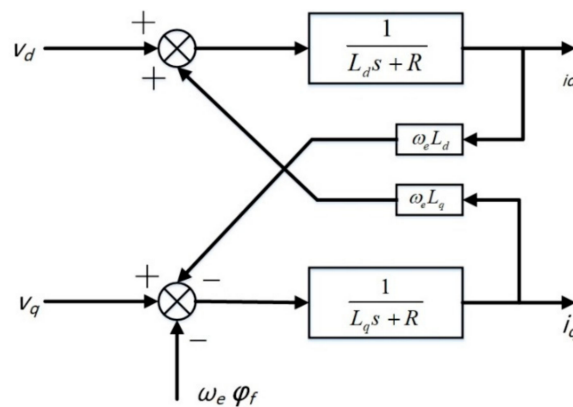


Figure 4. Dynamic block diagram of the PMSG.

2.3. LCL Filter

Due to the fact of its compact size and better performance in the attenuation of switching ripples, the LCL filter has received significant attention, especially in high-power applications. However, the LCL configuration can lead to resonance and, thus, instability problems [24,25]. Therefore, to ensure stable operation, the controller parameters should be carefully designed.

2.3.1. Two-Level Converter with LCL Filter

A three-phase, two-level voltage source converter (VSCs) with an LCL filter is shown in Figure 5a, while Figure 5b presents the equivalent single-phase LCL filter. The LCL filter is composed of the converter-side inductance (L_1) and its parasitic resistance (R_1), the grid-side inductance (L_2) and its parasitic resistance (R_2), the filter capacitance (C_f), the capacitor series resistance, and any added damping resistance (R_c). V_{conv} is the inverter output voltage, v_s is the grid-side voltage, L_s and R_s are the inductance and resistance of the source impedance of the grid bus to the point of common coupling (PCC), respectively, and v_{pcc} is the vector of the PCC phase voltage.

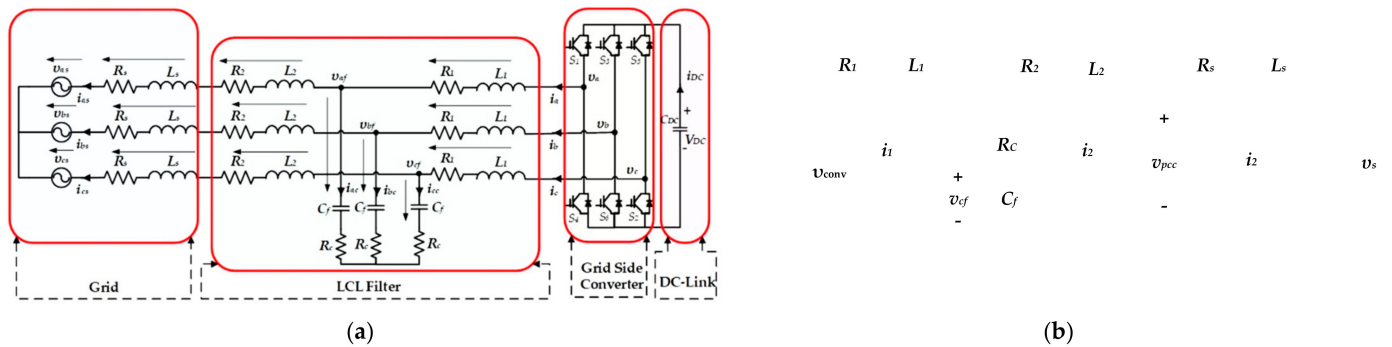


Figure 5. (a) A three-phase, two-level VSC with an LCL filter and (b) a single-phase LCL filter equivalent circuit.

The dynamic equations for the LCL filter can be written as follows:

$$\begin{cases} -v_{conv} + R_1 i_1 + R_c i_1 - R_c i_2 + L_1 \frac{di_1}{dt} + v_c = 0 \\ -v_c - R_c i_1 + R_c i_2 + R_2 i_2 + L_2 \frac{di_2}{dt} + v_{pcc} = 0 \\ i_1 - i_2 - C_f \frac{dv_c}{dt} = 0 \end{cases} \quad (9)$$

Rearranging the differential equations, the state-space model of the LCL filter can be written as follows:

$$\begin{cases} \dot{x} = Ax + Bu \\ y = Cx + Du \\ x(0) = x_0 \end{cases} \quad (10)$$

where

$$\begin{cases} x = y = \begin{bmatrix} i_1 \\ i_2 \\ v_c \end{bmatrix} \\ u = \begin{bmatrix} v_{conv} \\ v_{pcc} \end{bmatrix} \end{cases} \quad (11)$$

and

$$\left\{ \begin{aligned}
 A &= \begin{bmatrix} -\frac{R_1+R_c}{L_1} & \frac{R_c}{L_1} & -\frac{1}{L_1} \\ \frac{R_c}{L_2} & -\frac{R_2+R_c}{L_2} & \frac{1}{L_2} \\ \frac{1}{C_f} & -\frac{1}{C_f} & 0 \end{bmatrix} \\
 B &= \begin{bmatrix} \frac{1}{L_1} & 0 \\ 0 & -\frac{1}{L_2} \\ 0 & 0 \end{bmatrix} \\
 C &= \begin{bmatrix} 1 & 0 & 0 \\ 0 & 1 & 0 \\ 0 & 0 & 1 \end{bmatrix} \\
 D &= \begin{bmatrix} 0 & 0 & 0 \\ 0 & 0 & 0 \\ 0 & 0 & 0 \end{bmatrix}
 \end{aligned} \right. \tag{12}$$

Based on the previous mathematical model, the block diagram of the LCL filter was built as shown in Figure 6.

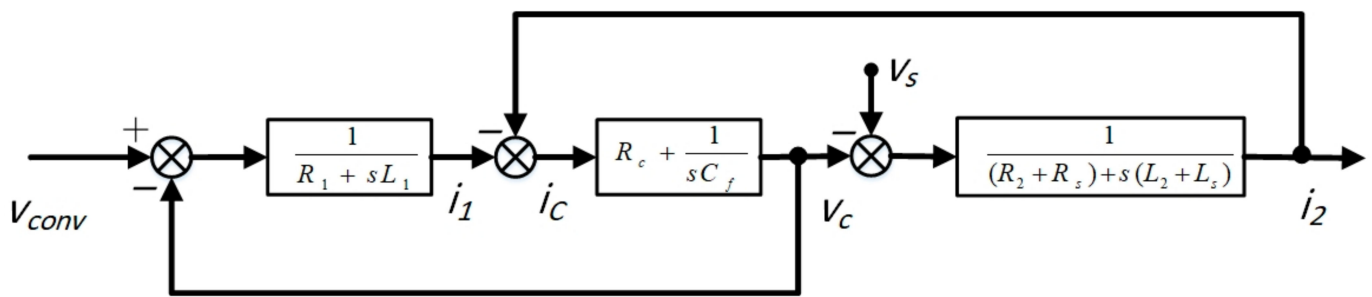


Figure 6. Laplace domain model of a grid converter with an LCL filter.

2.3.2. Filter Parameters Design

The parameter design of the LCL filter plays an essential role in transmitting high-quality power to the grid. In this paper, the design framework of the LCL filter had three main determinants:

1. The converter-side inductor was calculated based on the desired current ripple attenuation;
2. The filter capacitance (C_f) was designed based on the filter’s resonance frequency;
3. The capacitor series resistance (R_c) was selected based on the required damping factor.

The ripple current (ΔI_{Lmax}) was derived based on the worst case, where the maximum converter current ripple was obtained during the zero-crossing of the phase voltage [26,27], i.e., when the applied converter voltage varied from $\frac{V_{DC}}{3}$ to $-\frac{V_{DC}}{3}$ (see Figure 7):

$$\Delta I_{Lmax} = \frac{2V_{DC}}{3f_{sw}L_1} m(1 - m) \tag{13}$$

where f_{sw} is the switching frequency and m is the inverter modulation factor.

By selecting a maximum permissible current ripple (e.g., ($\Delta I_{Lmax} = 10\%$)), the required minimum converter-side inductor can be calculated according to the following equation:

$$L_{1min} = \frac{2V_{DC}}{3f_{sw} \Delta I_{Lmax}} m(1 - m) \tag{14}$$

The capacitor (C_f) was designed with the assumption that the reactive power (Q) was less than $\alpha\%$ of the rated power (P_{rat}), and α was a positive factor [28–30]:

$$\begin{cases} |Q| \leq (\alpha\%)P_{rat} \\ Q = -v_s^2 C_f \omega_g \end{cases} \tag{15}$$

where v_s is the stator RMS voltage, and ω_g is the grid angular frequency.

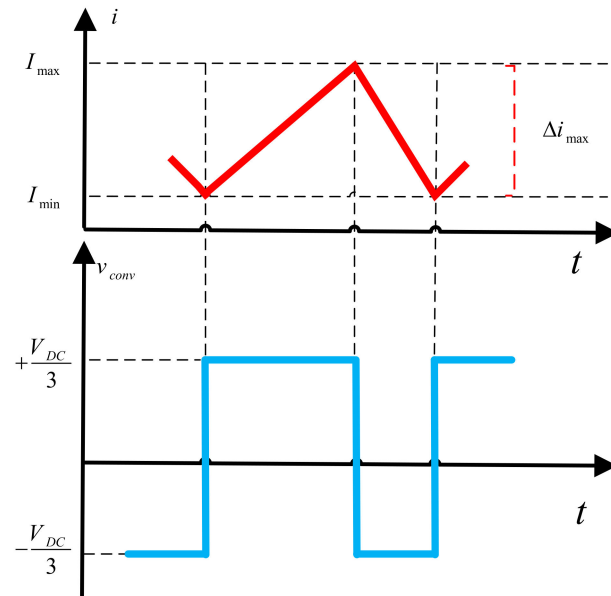


Figure 7. Current ripple by phase voltage zero-crossing.

The filter capacitor can be calculated as follows:

$$C_f = xC_b = x \frac{P_{rat}}{2\pi f_g v_s^2} \tag{16}$$

where C_b is the base capacitance calculated based on the nominal values of the voltage (V_{nom}), power (p_{nom}), and frequency (ω_{nom}) and x is the percentage of the reactive power absorbed under rated conditions (e.g., $x \leq 5\%$):

$$C_b = \frac{1}{\omega_{nom} Z_b}, Z_b = \frac{V_{nom}^2}{P_{nom}} \tag{17}$$

The grid-side inductor L_2 was selected according to the grid code requirements related to the harmonic current limits. It can be calculated based on the current ripple attenuation (δ). The current ripple attenuation was defined as the ratio of grid current (i_2) to the converter output current (i_1):

$$\frac{i_2(f_{sw})}{i_1(f_{sw})} = \delta = \frac{1}{|1 + \beta(1 - xL_1C_b\omega_{sw}^2)|} \tag{18}$$

where $\beta = \frac{L_2}{L_1}$.

To avoid resonance problems, the resonance frequency (f_{res}) should be in the range of 10 times the grid frequency (f_g) and one-half of the switching frequency (f_{sw}) [31]:

$$10f_g \leq f_{res} \leq \frac{1}{2}f_{sw} \tag{19}$$

where

$$\begin{cases} f_{res} = \frac{\omega_{res}}{2\pi} \\ \omega_{res} = \sqrt{\frac{L_1+L_2}{L_1L_2C_f}} \end{cases} \tag{20}$$

Finally, adding a passive damping resistor (R_c) ensures a more stable operation of the LCL filter. According to previous work [31,32], the damping resistor was chosen as one-third of the impedance of the capacitors at resonant frequency:

$$R_c = \frac{1}{6\pi f_{res} C_f} \quad (21)$$

2.4. Modeling of the DC Link

The DC link is represented as a shunt capacitance connected between the MSC and GSC as depicted in Figure 8.

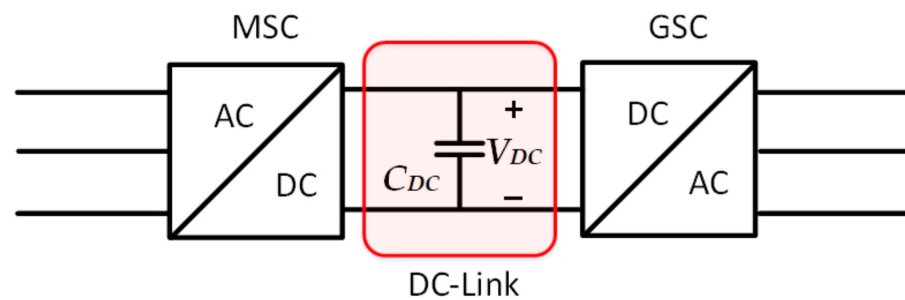


Figure 8. DC-link model.

The energy stored (W_{DC}) in the DC-link can be estimated as follows:

$$W_c = \frac{1}{2} C_{DC} (V_{DC}^2) \quad (22)$$

Based on the maximum permissible voltage ripple, the DC-link capacitance can be selected. The voltage ripple (ΔV_{DC}) depends on the DC-link capacitor size and switching frequency. The DC-link capacitor (C_{DC}) is expressed as follows [33]:

$$C_{DC} \geq \frac{P_{nom}}{4\sqrt{3}\pi f V_{DC} \Delta V_{DC}} \quad (23)$$

where P_{nom} is the nominal power of the voltage source converter (VSC), and f is the fundamental frequency of the AC power supply. In this work, the allowed DC-link voltage ripple was $\Delta V_{DC} \approx 5\%$ of V_{DC} .

3. Control of the GSC

The main purpose of a GSC controller is to stabilize the DC-link voltage and control the reactive power flowing from or to the grid, i.e., the unity power factor [34]. The active and reactive power can be controlled by the direct and quadratic current using grid voltage-oriented control (VOC). On the VOC, the grid voltage is aligned to the d -axis, as depicted in Figure 9, allowing for decoupled control of the active and reactive power flowing between the GSC and the grid.

The detailed control structure of the VOC is shown in Figure 10. Two inner and outer loops were used to control the GSC. The outer loop was used to adjust the DC-link voltage and the reactive power for the grid side, while the inner loop was used to control the power at the grid side.

Assuming the LCL filter resonance frequency was much lower than the switching frequency, the LCL filter can be considered an RL filter [24,35]. Based on this approximation, the resistance and inductance of the modified model of the LCL filter can be expressed as:

$$\begin{cases} R_f = R_1 + R_2 \\ L_f = L_1 + L_2 \end{cases} \quad (24)$$

where R_f and L_f are the resistance and inductance of the equivalent RL filter, respectively.

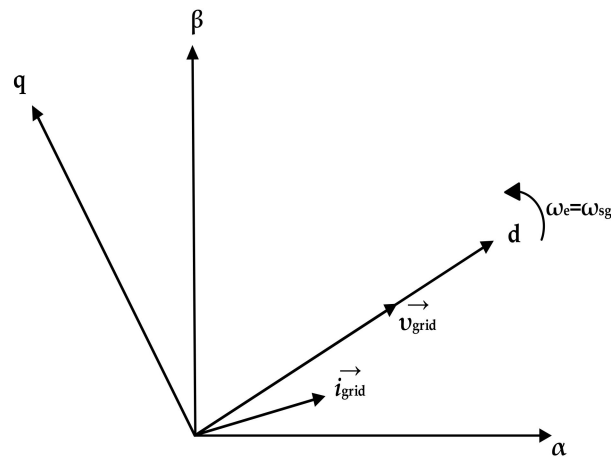


Figure 9. Schematic of the space vectors.

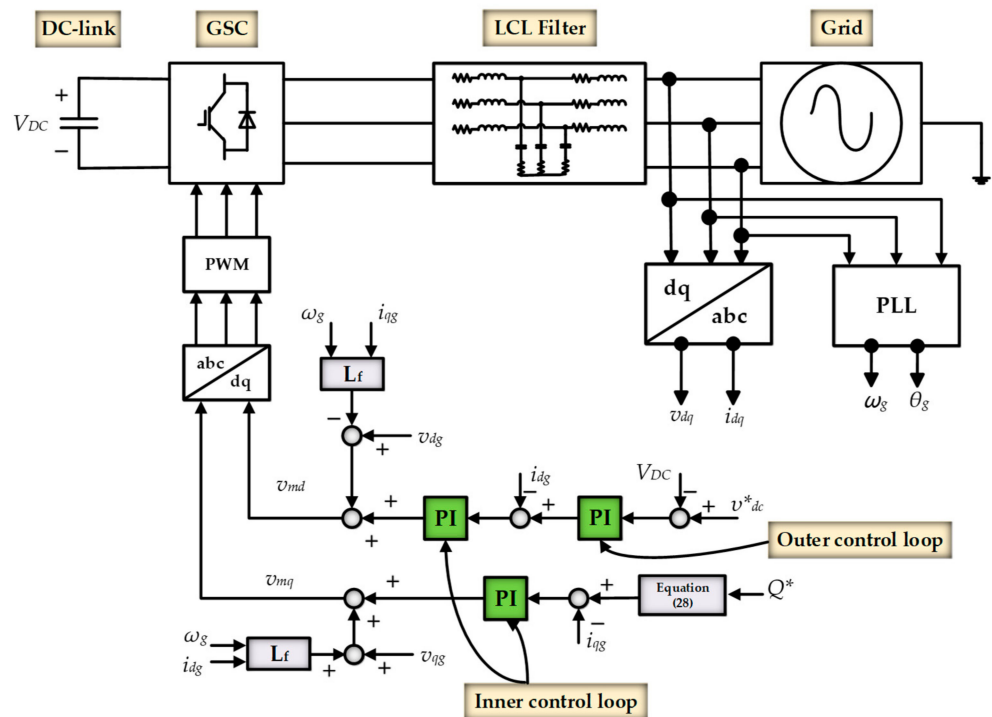


Figure 10. Voltage-oriented control of the GSC.

Using the modified filter model, the voltage and current relationship between the grid and the converter output can be expressed as follows:

$$v_{dg} = v_{di} - L_f \frac{di_{dg}}{dt} - R_f i_{dg} + \omega_g L_f i_{qg} \tag{25}$$

$$v_{qg} = v_{qi} - L_f \frac{di_{qg}}{dt} - R_f i_{qg} - \omega_g L_f i_{dg} \tag{26}$$

where v_{dg} and v_{qg} are the dq-axis components of the grid voltages; i_{dg} and i_{qg} are the dq-axis components of the grid currents; v_{di} and v_{qi} are the dq-axis components of the converter voltages.

While decoupled active and reactive power control was performed by aligning the grid voltage to the d -axis (i.e., $v_{qi} = 0$), the active and reactive power was solely related to the d -axis and q -axis current through the grid filter:

$$P_{grid} = \frac{3}{2} (v_{dg} i_{dg}) \quad (27)$$

$$Q_{grid} = -\frac{3}{2} (v_{dg} i_{qg}) \quad (28)$$

where P_{grid} and Q_{grid} are the active and reactive powers of the grid-side converter, respectively. The DC-link voltage can be easily controlled through the d -axis current, i_{dg} , as follows:

$$C \frac{dv_{DC}}{dt} = i_{DC} - \frac{3}{2} \frac{v_{dg}}{v_{DC}} i_{dg} \quad (29)$$

Furthermore, the synchronous reference frame phase-locked loop (SRF-PLL) was used to calculate the grid-side phase angle (θ_g) and grid angular frequency (ω_g). As the d -axis grid voltage was aligned to the d -axis, the calculated angle was adjusted until the q -axis grid voltage became zero.

As previously mentioned, the GSC controller scheme was implemented with two current-control loops. Firstly, the d -axis current was used to regulate the DC-bus voltage. The difference between the reference and the measured values of the DC-link voltage was amplified by the PI regulator, resulting in the d -axis current reference (i_{gd}^{ref}). Subsequently, the i_{gd} was controlled to track the i_{gd}^{ref} through the PI regulator. A compensation (decoupling) was used to eliminate the coupling between the d -axis and q -axis current controls. Based on that, the output of the PI regulator was added to a compensation term and, thus, the d -axis reference voltage of the converter v_{md} was obtained.

The second control loop was the reactive-power control loop, which was controlled through the q -axis current, i_{qg} , see Figure 10. The q -axis current reference (i_{qg}^{ref}) was calculated based on (28). A PI regulator was used to control the q -axis current (i_{qg}). Finally, the q -axis reference voltage of the converter (v_{mq}) was obtained by adding the output of the PI regulator to the compensation term. Once the reference voltages v_{mq} and v_{md} were obtained and transformed into the abc frame, the PWM pulses were generated and fed to the grid converter.

4. Direct Torque Control (DTC)

4.1. Conventional 6-Sectors DTC

DTC directly controls the stator flux and electromagnetic torque by selecting the appropriate converter state. A complete block diagram of the DTC is shown in Figure 11. As shown, the reference values for the stator flux and electromagnetic torque were compared to the estimated values to produce the error of the stator flux and torque, which were transferred to their respective hysteresis comparators.

The stator flux was controlled through a two-level hysteresis comparator, while the electromagnetic torque was controlled using a three-level hysteresis comparator as shown in Figure 12.

The hysteresis comparators generate the required hysteresis band of flux and torque, and then the optimal vector voltage is selected. In this case, the optimal vector voltage was generated by the MSC to track the required increase or decrease in the torque and flux variables.

As shown in Figure 12, the output of the torque hysteresis band controller is represented by the variable H_{Tem} , which refers to increased ($HT = 1$), decreased ($HT = -1$), or constant ($HT = 0$), depending on the input.

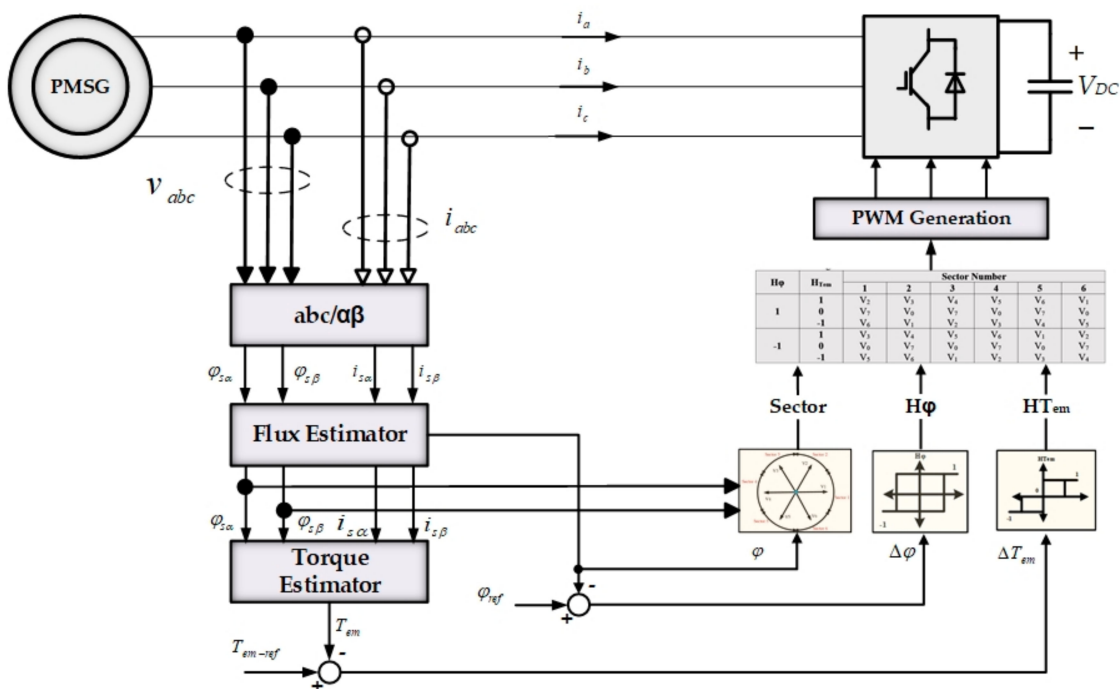


Figure 11. Conventional 6-sectors DTC.

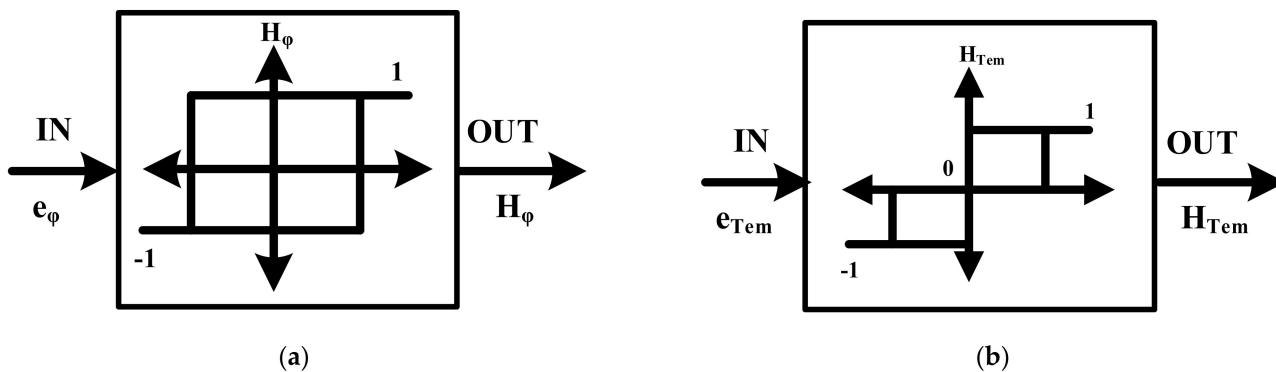


Figure 12. (a) A two-level hysteresis comparator for stator flux control and (b) a three-level hysteresis comparator for torque control.

Since the DTC keeps the amplitude of the stator flux vector at a near-constant value for fixed time intervals, and assuming that the stator resistance (R) voltage drop was neglected (i.e., the stator voltage remained constant), the stator voltage directly affected the stator flux according to the following equation:

$$\Delta\varphi_i(t) = \varphi_i(t) - \varphi_i(t - \Delta t) = \int_{t-\Delta t}^t v_i \Delta t \cong v_i \Delta t \tag{30}$$

By selecting the right voltage vector (v_i) for each time interval (Δt), it is possible to estimate the flux (φ_i) and, thus, the electromagnetic torque can be calculated as a result of the equation presented below (34). The voltage vector plane was divided into six sectors, as shown in Figure 13, while the optimal voltage vector was selected based on the switching table shown in Table 1.

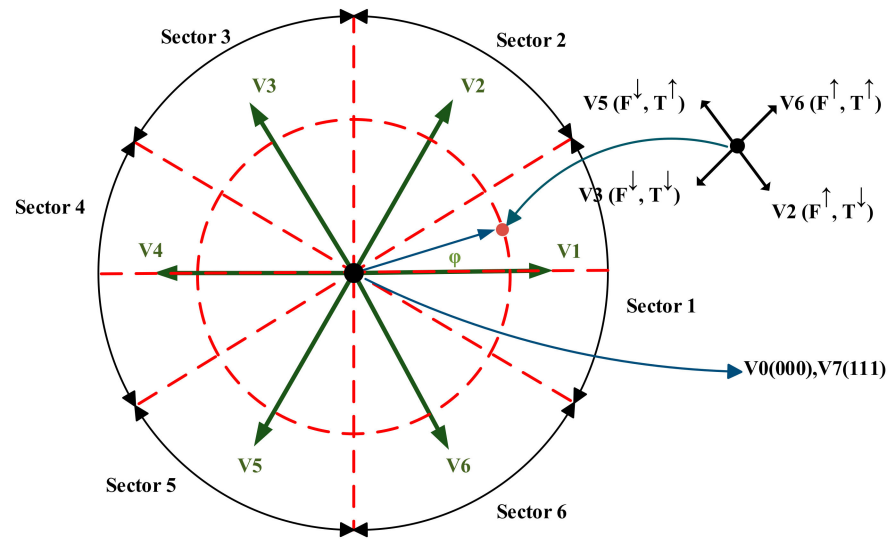


Figure 13. Voltage vectors in the 6-sectors DTC.

Table 1. Switching Table of the 6-sectors DTC.

Hφ	HTem	Sector Number					
		1	2	3	4	5	6
1	1	V ₂	V ₃	V ₄	V ₅	V ₆	V ₁
	0	V ₇	V ₀	V ₇	V ₀	V ₇	V ₀
	-1	V ₆	V ₁	V ₂	V ₃	V ₄	V ₅
-1	1	V ₃	V ₄	V ₅	V ₆	V ₁	V ₂
	0	V ₀	V ₇	V ₀	V ₇	V ₀	V ₇
	-1	V ₅	V ₆	V ₁	V ₂	V ₃	V ₄

4.2. Torque and Flux Reference Values Definition

It is well known that the stator flux can be estimated through the voltage and current of the stator [1].

$$\begin{cases} \varphi_{s\alpha} = \int (v_{s\alpha} - Ri_{s\alpha}) dt \\ \varphi_{s\beta} = \int (v_{s\beta} - Ri_{s\beta}) dt \end{cases} \quad (31)$$

where $\varphi_{s\alpha}$ and $\varphi_{s\beta}$ are the $\alpha\beta$ -axis components of the stator fluxes; $v_{s\alpha}$ and $v_{s\beta}$ are the $\alpha\beta$ -axis components of the stator voltages; $i_{s\alpha}$ and $i_{s\beta}$ are the $\alpha\beta$ -axis components of the stator currents, see Figure 9.

Based on Equation (31), the magnitude ($|\varphi_s|$) and angle position of the stator flux vector (θ_s) can be calculated as follows:

$$|\varphi_s| = \sqrt{\varphi_{s\alpha}^2 + \varphi_{s\beta}^2} \quad (32)$$

$$\theta_s = \tan^{-1} \left(\frac{\varphi_{s\beta}}{\varphi_{s\alpha}} \right) \quad (33)$$

The flux reference (φ_{ref}) was obtained using a lookup table. The lookup table provides the φ_{ref} as a function of the speed (ω_r). In this work, the flux was assumed as a constant value, rated value (φ_{rated}), during the operation in the range of the nominal speed (ω_{nom}). Conversely, as the speed becomes higher than the base speed, the flux should be reduced:

$$\begin{cases} \varphi_{ref} = \varphi_{rated} & \text{for } \omega_r < \omega_{nom} \\ \varphi_{ref} = \varphi_{rated} \left(\frac{\omega_{nom}}{\omega_r} \right) & \text{for } \omega_r > \omega_{nom} \end{cases} \quad (34)$$

The torque reference is generated from the speed controller and then compared to the estimated torque. In this paper (see Section 5), the torque reference was assumed to be constant over a certain interval of time and modeled as a time step function. According to previous research [1,36], the electromagnetic torque can be estimated as follows:

$$T_{em} = \frac{3}{2}p(\varphi_{s\alpha}i_{s\beta} - \varphi_{s\beta}i_{s\alpha}) \tag{35}$$

4.3. Proposed 12-Sectors DTC of the PMSG

The main disadvantages of the conventional 6-sectors DTC are the variable switching frequency, the high-current total harmonic distortion (THD), the high torque ripples, and the problem of flux drop at low speeds [37,38].

Furthermore, in conventional DTC, two states of presented torque are not used (see Table 1). The voltage vectors V_1 and V_4 do not exist in the first sector, and that is right for the other sectors with different voltage vectors. This leads to inaccuracy in the torque and flux within a 60° sector. In this paper, to overcome these drawbacks, a 12-sectors DTC is proposed, where the sector number is increased to 12 sectors of 30° for each sector rather than 60° .

Table 2 shows the possible voltage vector combinations in the proposed 12-sectors DTC technique, where $H_{T_{em}} = 2, -2 (T^{\uparrow\uparrow}, T^{\downarrow\downarrow})$ represents a large increase and decrease in torque; $H_{T_{em}} = 1, -1 (T^{\uparrow}, T^{\downarrow})$ represents a small increase and decrease in torque; $H_\varphi = 1, -1 (\varphi^{\uparrow}, \varphi^{\downarrow})$ represents an increase and decrease in flux. The voltage vector plane was divided into 12 sectors, as illustrated in Figure 14.

Table 2. Switching table for the proposed 12-sectors DTC.

H_φ	$H_{T_{em}}$	Sector Number											
		1	2	3	4	5	6	7	8	9	10	11	12
1	2	V_2	V_3	V_3	V_4	V_4	V_5	V_5	V_6	V_6	V_1	V_1	V_2
	1	V_2	V_2	V_3	V_3	V_4	V_4	V_5	V_5	V_6	V_6	V_1	V_1
	-1	V_1	V_1	V_2	V_2	V_3	V_3	V_4	V_4	V_5	V_5	V_6	V_6
	-2	V_6	V_1	V_1	V_2	V_2	V_3	V_3	V_4	V_4	V_5	V_5	V_6
-1	2	V_3	V_4	V_4	V_5	V_5	V_6	V_6	V_1	V_1	V_2	V_2	V_3
	1	V_4	V_4	V_5	V_5	V_6	V_6	V_1	V_1	V_2	V_2	V_3	V_3
	-1	V_7	V_5	V_0	V_6	V_7	V_1	V_0	V_2	V_7	V_3	V_0	V_4
	-2	V_5	V_6	V_6	V_1	V_1	V_2	V_2	V_3	V_3	V_4	V_4	V_5

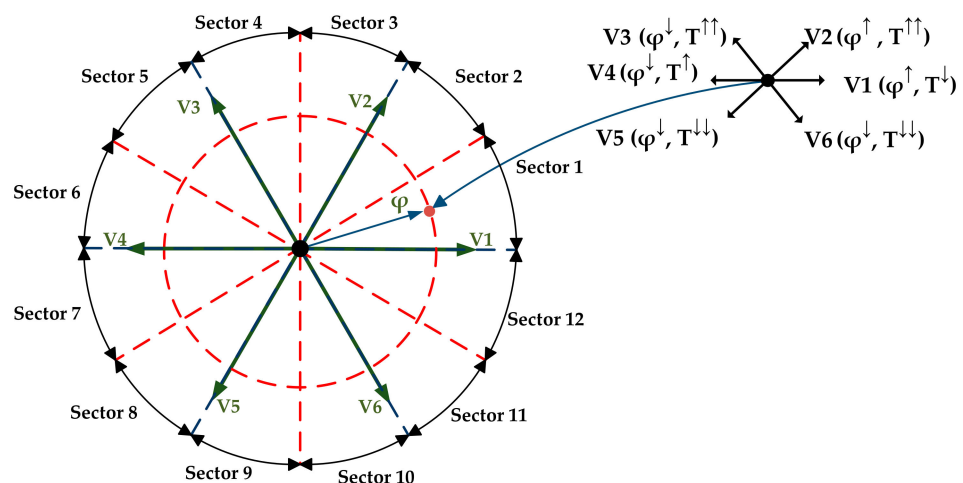


Figure 14. Voltage vectors in the proposed 12-sectors DTC.

Generally, the sector (s_x) can be determined as follows:

$$\frac{\pi(m-1)}{6} \leq s_x < \frac{\pi m}{6} \quad (36)$$

where m is the sector number ($m = 1, 2, \dots, 12$).

In this approach, a four-level hysteresis comparator was applied to the torque, and a two-level was used for the flux. The following conditions were used in the torque comparator:

$$\begin{cases} H_{Tem} = 2 \rightarrow \Delta T_{em} \geq \frac{HB_T}{2} \\ H_{Tem} = 1 \rightarrow \frac{HB_T}{2} \geq \Delta T_{em} \geq 0 \\ H_{Tem} = -1 \rightarrow -\frac{HB_T}{2} \leq \Delta T_{em} \leq 0 \\ H_{Tem} = -2 \rightarrow \Delta T_{em} \leq -\frac{HB_T}{2} \end{cases} \quad (37)$$

where H_{Tem} is the torque status signal; ΔT_{em} is the difference between the reference and actual values of electromagnetic torque ($\Delta T_{em} = T_{em-ref} - T_{em}$); HB_T is the hysteresis band of the torque.

5. Results and Discussion

To verify the proposed 12-sectors DTC control strategy, a MATLAB/Simulink-based simulation was carried out. The nominal parameters of the 3.5 kW system are listed in Table 3.

Table 3. 3.5 kW PMSG parameters.

Parameter	Value
Rated power, P_n	3.5 kW
Power frequency, f_n	50 Hz
Number of pole pairs, P	4
Stator voltage, V_{Grid}	380 V
Nominal torque, T_n	23.7 N·m
Stator resistance, R	0.997 Ω
Maximum switching frequency, f_{sw-MAX}	20 kHz

In the simulation, the torque hysteresis band was selected as 5% T_n , and the flux hysteresis band value was set at 2% φ . The DC-link was kept at approximately 1200 V. The sampling time of both DTC algorithms was 50 μ s.

The reference torque was selected as a function of time, as depicted in Figure 15. As shown, for the conventional 6-sectors DTC and the proposed 12-sectors DTC, the simulated torque followed its reference well, with notable ripples. Conversely, the reference was reached quickly, i.e., settling time $\approx 810 \mu$ s for the 6-sectors DTC and $\approx 700 \mu$ s for the 12-sectors DTC. This confirms the advantages of the fast torque response of DTC techniques.

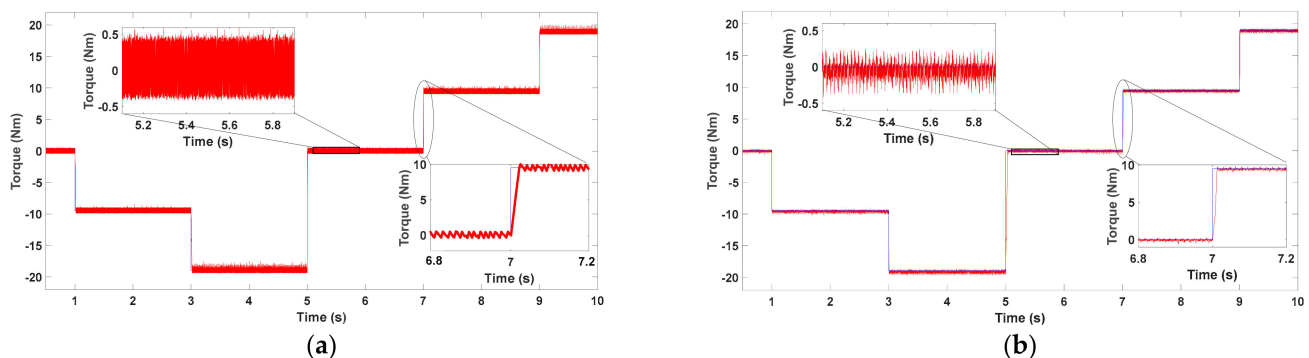


Figure 15. Electromagnetic torque response with (a) 6–sectors and (b) 12–sectors DTC control strategies.

Further, Figure 16 depicts the stator flux, which attracted its reference well. The trajectory of the stator flux vector is presented in Figure 17. From Figure 17, it is clear that the stator flux vector rotated with a constant magnitude and small oscillation.

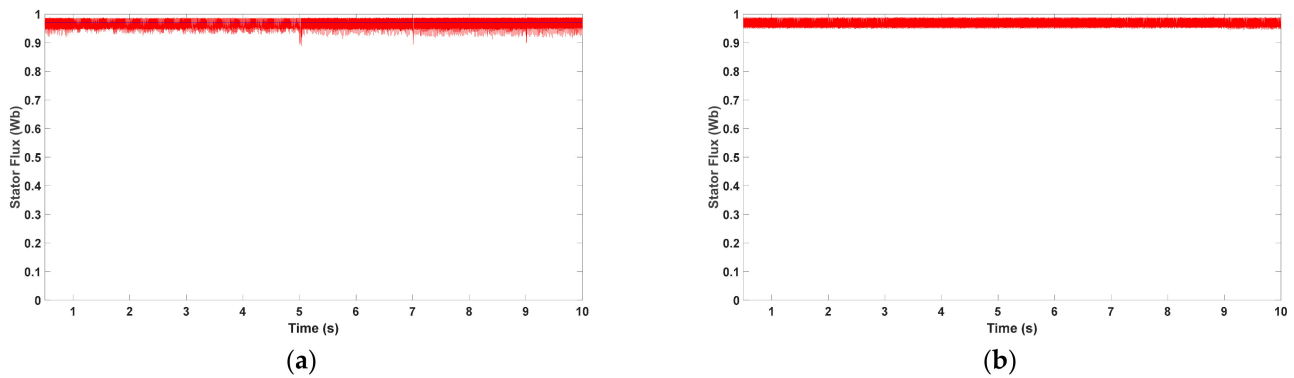


Figure 16. Stator flux response with (a) 6-sectors and (b) 12-sectors DTC control strategies.

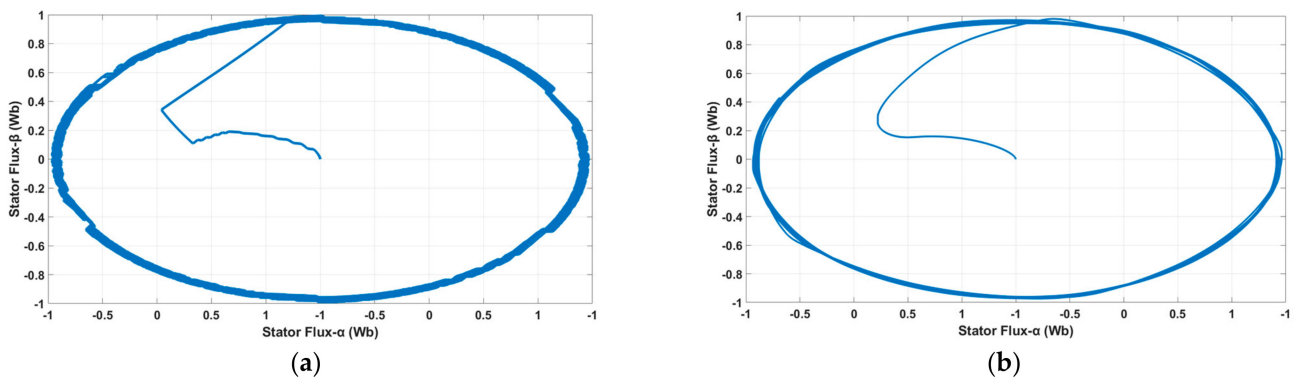


Figure 17. Stator flux trajectory with (a) 6-sectors and (b) 12-sectors DTC control strategies.

However, the main drawback of DTC is the ripple in torque and flux due to the variable switching frequency. As shown in Figure 15, in the comparative results between the 6-sectors and 12-sectors DTCs, the dynamic responses were almost the same, but the torque and flux ripples during transient and steady-state were clearly reduced in the proposed 12-sectors method.

Table 4 presents the ripples percentage of torque and flux at different reference torque values. As expected, both DTC algorithms had ripples in torque and flux, and it is clear that the 12-sectors DTC had the best performance, as the ripples were significantly reduced over a wide operation range.

Table 4. Comparative analysis of torque and flux ripples for different DTC algorithms.

T_{ref}	6-Sectors DTC		12-Sectors DTC	
	T_{ripple}	φ_{ripple}	T_{ripple}	φ_{ripple}
$-0.8 \cdot T_n$	8.72%	4.22%	2.95%	2.35%
$-0.4 \cdot T_n$	7.33%	3.10%	5.23%	2.10%
$+0.8 \cdot T_n$	10.72%	7.22%	2.11%	3.11%
$+0.4 \cdot T_n$	9.82%	8.12%	3.26%	2.21%

In the conventional 6-sectors DTC, and due to the fact that two states of the presented torque were not used, the torque control was ambiguous. This resulted in high ripples in the torque and flux, see Table 4.

Conversely, applying the 12-sectors strategy guaranteed that all voltage vectors were used and, therefore, the switching was more accurate and had a good dynamic response.

Further, using twelve 30° sectors for voltage and flux vectors and applying the four-level hysteresis comparator (i.e., a large increase and decrease, a small increase and decrease in torque) provided additional degrees of freedom to select the optimal voltage vectors. This was mainly because the number of sectors was the most influential factor in reducing ripples and, hence, smooth operation.

The steady-state response of the stator voltages is presented in Figure 18. Figure 19 presents the stator flux sectors for both techniques, where the main difference is the sectors' division with respect to time.

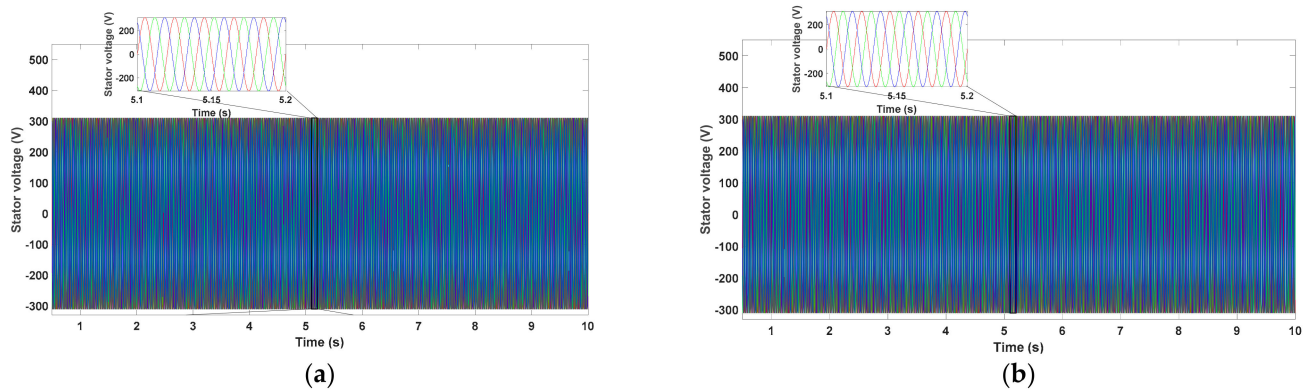


Figure 18. Stator voltage response with (a) 6–sectors and (b) 12–sectors DTC control strategies.

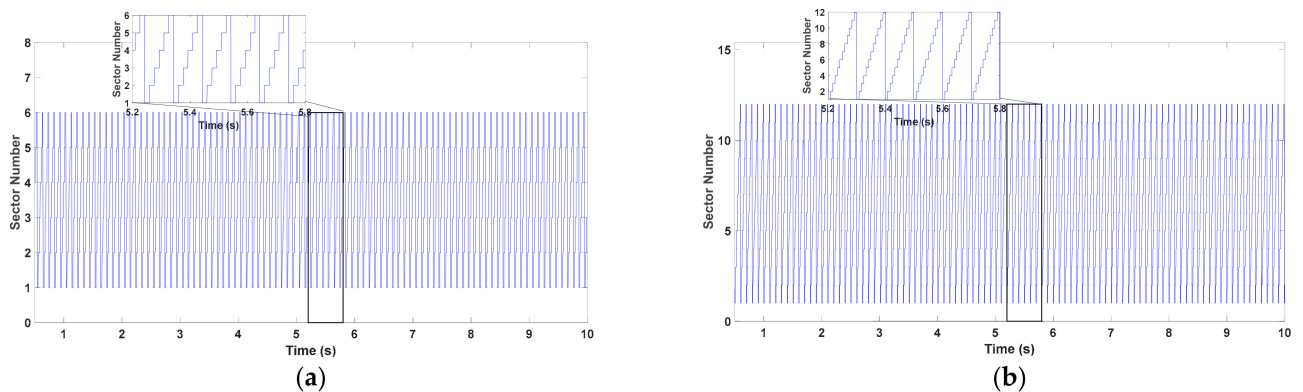


Figure 19. Stator flux sectors with (a) 6–sectors and (b) 12–sectors DTC control strategies.

To achieve a deeper analysis of the discussed DTC techniques, the fast Fourier transform (FFT) was applied to the stator currents in order to determine the current total harmonic distortion (THD). The results are presented in Figure 20, and they show that the THD of the stator current was 12.40% and 3.30% for the 6-sectors and 12-sectors DTC, respectively.

It is clear from the analysis that the 12-sectors DTC had the best performance and the least number of ripples when compared to the conventional 6-sectors DTC. The considerable simplicity, reduction in torque and flux ripples, good dynamic responses, and low THD of the 12-sectors controller verify its effectiveness. Conversely, due to the increase in the size of the switching table, the computational complexity was prominent when using the 12-sectors control scheme.

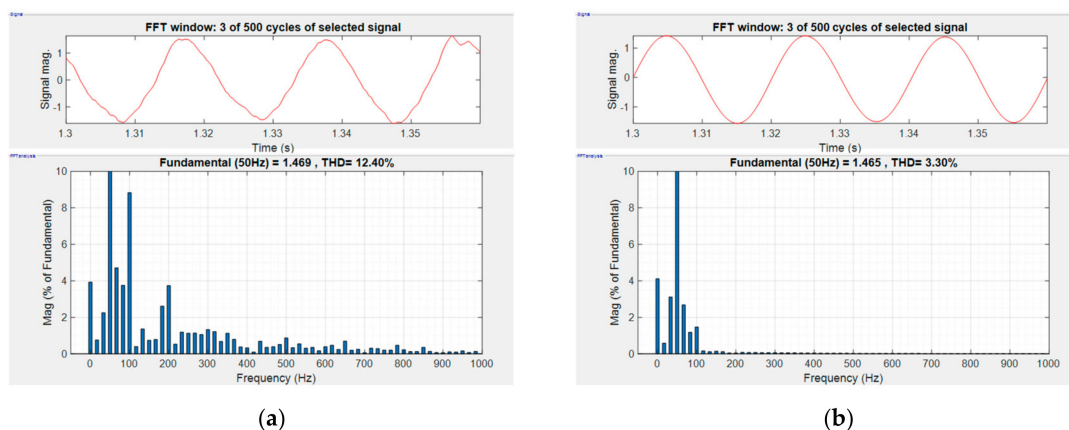


Figure 20. The FFT analysis of the phase-a stator current with (a) 6–sectors and (b) 12–sectors DTC control strategies.

6. Conclusions

The dynamic modeling and control approach of a WECS with a variable-speed direct-driven PMSG was presented in this paper. Through this, a new 12–sectors DTC control technique for PMSG-based wind turbines was proposed. The principle of the 6–sectors DTC control algorithm was first investigated, and, subsequently, the proposed DTC technique was presented in order to improve the performance and overcome the disadvantages of the conventional method. The simulations were carried out in the MATLAB/Simulink environment, and the characteristics of the PMSG for both the DTC algorithms were discussed and compared.

Compared to the conventional 6–sectors method, the proposed 12–sectors DTC showed more satisfactory performance with a considerable reduction in flux and torque ripples, good dynamic performance, low THD and, thus, the best output characteristics.

Future work can extend the current study by implementing the proposed control technique in an FPGA-based control system.

Funding: This research received no external funding.

Institutional Review Board Statement: Not applicable.

Informed Consent Statement: Not applicable.

Data Availability Statement: Not applicable.

Conflicts of Interest: The authors declare no conflict of interest.

References

1. Rasul, M.G.; Azad, A.K.; Sharma, S.C. *Clean Energy for Sustainable Development Comparisons and Contrasts of New Approaches*; Academic Press is an imprint of Elsevier: Amsterdam, The Netherlands, 2017; ISBN 978-0-12-805423-9.
2. Polinder, H.; van der Pijl, F.; de Vilder, G.-J.; Tavner, P.J. Comparison of Direct-Drive and Geared Generator Concepts for Wind Turbines. *IEEE Trans. Energy Convers.* **2006**, *21*, 725–733. [[CrossRef](#)]
3. Wu, B.; Xu, D.; Ji, J.; Zhao, W.; Jiang, Q. Field-oriented control and direct torque control for a five-phase fault-tolerant flux-switching permanent-magnet motor. *Chin. J. Electr. Eng.* **2018**, *4*, 48–56. [[CrossRef](#)]
4. Busca, C.; Stan, A.-I.; Stanciu, T.; Stroe, D.I. Control of Permanent Magnet Synchronous Generator for large wind turbines. In Proceedings of the 2010 IEEE International Symposium on Industrial Electronics (ISIE 2010), Bari, Italy, 4 July 2010–7 July 2010; pp. 3871–3876.
5. Abosh, A.H.; Zhu, Z.Q.; Ren, Y. Reduction of Torque and Flux Ripples in Space Vector Modulation-Based Direct Torque Control of Asymmetric Permanent Magnet Synchronous Machine. *IEEE Trans. Power Electron.* **2017**, *32*, 2976–2986. [[CrossRef](#)]
6. Kim, S.J.; Kim, J.-W.; Park, B.-G.; Lee, D.-H. A Novel Predictive Direct Torque Control Using an Optimized PWM Approach. *IEEE Trans. Ind. Appl.* **2021**, *57*, 2537–2546. [[CrossRef](#)]
7. Guo, L.; Zhang, X.; Yang, S.; Xie, Z.; Wang, L.; Cao, R. Simplified model predictive direct torque control method without weighting factors for permanent magnet synchronous generator-based wind power system. *IET Electr. Power Appl.* **2017**, *11*, 793–804. [[CrossRef](#)]

8. Preindl, M.; Bolognani, S. Model Predictive Direct Torque Control With Finite Control Set for PMSM Drive Systems, Part 1: Maximum Torque Per Ampere Operation. *IEEE Trans. Ind. Inf.* **2013**, *9*, 1912–1921. [[CrossRef](#)]
9. Yaramasu, V.; Wu, B. Predictive Control of a Three-Level Boost Converter and an NPC Inverter for High-Power PMSG-Based Medium Voltage Wind Energy Conversion Systems. *IEEE Trans. Power Electron.* **2014**, *29*, 5308–5322. [[CrossRef](#)]
10. Golnary, F.; Moradi, H. Dynamic modelling and design of various robust sliding mode controls for the wind turbine with estimation of wind speed. *Appl. Math. Model.* **2019**, *65*, 566–585. [[CrossRef](#)]
11. Beltran, B.; Benbouzid, M.E.H.; Ahmed-Ali, T. Second-Order Sliding Mode Control of a Doubly Fed Induction Generator Driven Wind Turbine. *IEEE Trans. Energy Convers.* **2012**, *27*, 261–269. [[CrossRef](#)]
12. Do, T.D. Disturbance Observer-Based Fuzzy SMC of WECSs Without Wind Speed Measurement. *IEEE Access* **2017**, *5*, 147–155. [[CrossRef](#)]
13. Watil, A.; El Magri, A.; Raihani, A.; Lajouad, R.; Giri, F. Multi-objective output feedback control strategy for a variable speed wind energy conversion system. *Int. J. Electr. Power Energy Syst.* **2020**, *121*, 106081. [[CrossRef](#)]
14. Errami, Y.; Ouassaid, M.; Maaroufi, M. A performance comparison of a nonlinear and a linear control for grid connected PMSG wind energy conversion system. *Int. J. Electr. Power Energy Syst.* **2015**, *68*, 180–194. [[CrossRef](#)]
15. Zhang, Z.; Wang, F.; Si, G.; Kennel, R. Predictive encoderless control of back-to-back converter PMSG wind turbine systems with Extended Kalman Filter. In Proceedings of the 2016 IEEE 2nd Annual Southern Power Electronics Conference (SPEC), Auckland, New Zealand, 5 December 2016–8 December 2016; pp. 1–7.
16. Mousa, H.H.; Youssef, A.-R.; Mohamed, E.E. Hybrid and adaptive sectors P&O MPPT algorithm based wind generation system. *Renew. Energy* **2020**, *145*, 1412–1429. [[CrossRef](#)]
17. Shang, L.; Hu, J. Sliding-Mode-Based Direct Power Control of Grid-Connected Wind-Turbine-Driven Doubly Fed Induction Generators Under Unbalanced Grid Voltage Conditions. *IEEE Trans. Energy Convers.* **2012**, *27*, 362–373. [[CrossRef](#)]
18. Toumi, I.; Meghni, B.; Hachana, O.; Azar, A.T.; Boulmaiz, A.; Humaidi, A.J.; Ibraheem, I.K.; Kamal, N.A.; Zhu, Q.; Fusco, G.; et al. Robust Variable-Step Perturb-and-Observe Sliding Mode Controller for Grid-Connected Wind-Energy-Conversion Systems. *Entropy* **2022**, *24*, 731. [[CrossRef](#)]
19. Fateh, F.; White, W.N.; Gruenbacher, D. A Maximum Power Tracking Technique for Grid-Connected DFIG-Based Wind Turbines. *IEEE J. Emerg. Sel. Top. Power Electron.* **2015**, *3*, 957–966. [[CrossRef](#)]
20. Abdellatif, W.S.E.; Hamada, A.M.; Abdelwahab, S.A.M. Wind speed estimation MPPT technique of DFIG-based wind turbines theoretical and experimental investigation. *Electr Eng* **2021**, *103*, 2769–2781. [[CrossRef](#)]
21. Nasiri, M.; Milimonfared, J.; Fathi, S.H. A review of low-voltage ride-through enhancement methods for permanent magnet synchronous generator based wind turbines. *Renew. Sustain. Energy Rev.* **2015**, *47*, 399–415. [[CrossRef](#)]
22. Ashourianjozdani, M.; Lopes, L.A.C.; Pillay, P. Power Electronic Converter Based PMSG Emulator: A Testbed for Renewable Energy Experiments. *IEEE Trans. Ind. Appl.* **2018**, *54*, 3626–3636. [[CrossRef](#)]
23. Prakash, M.; Joo, Y.-H. Fuzzy Event-triggered Control for Back to Back Converter involved PMSG-based Wind Turbine Systems. *IEEE Trans. Fuzzy Syst.* **2021**, *30*, 1409–1420. [[CrossRef](#)]
24. Said-Romdhane, M.; Naouar, M.; Belkhodja, I.; Monmasson, E. An Improved LCL Filter Design in Order to Ensure Stability without Damping and Despite Large Grid Impedance Variations. *Energies* **2017**, *10*, 336. [[CrossRef](#)]
25. Teodorescu, R.; Liserre, M.; Rodríguez, P. *Grid Converters for Photovoltaic and Wind Power Systems*; Wiley: Chichester, UK, 2011. ISBN 047066 7052.
26. Reznik, A.; Simoes, M.G.; Al-Durra, A.; Muyeen, S.M. LCL Filter Design and Performance Analysis for Grid-Interconnected Systems. *IEEE Trans. Ind. Appl.* **2014**, *50*, 1225–1232. [[CrossRef](#)]
27. Lu, M.; Al-Durra, A.; Muyeen, S.M.; Leng, S.; Loh, P.C.; Blaabjerg, F. Benchmarking of Stability and Robustness Against Grid Impedance Variation for LCL -Filtered Grid-Interfacing Inverters. *IEEE Trans. Power Electron.* **2018**, *33*, 9033–9046. [[CrossRef](#)]
28. Sanatkar-Chayjani, M.; Monfared, M. Design of LCL and LLCL filters for single-phase grid connected converters. *IET Power Electron.* **2016**, *9*, 1971–1978. [[CrossRef](#)]
29. Xue, C.; Zhou, D.; Li, Y. Hybrid Model Predictive Current and Voltage Control for LCL-Filtered Grid-Connected Inverter. *IEEE J. Emerg. Sel. Top. Power Electron.* **2021**, *9*, 5747–5760. [[CrossRef](#)]
30. Rockhill, A.A.; Liserre, M.; Teodorescu, R.; Rodríguez, P. Grid-Filter Design for a Multimegawatt Medium-Voltage Voltage-Source Inverter. *IEEE Trans. Ind. Electron.* **2011**, *58*, 1205–1217. [[CrossRef](#)]
31. Liserre, M.; Blaabjerg, F.; Hansen, S. Design and Control of an LCL-Filter-Based Three-Phase Active Rectifier. *IEEE Trans. Ind. Appl.* **2005**, *41*, 1281–1291. [[CrossRef](#)]
32. Zhan, P.; Lin, W.; Wen, J.; Yao, M.; Li, N. Design of LCL filters for the back-to-back converter in a Doubly Fed Induction Generator. In Proceedings of the IEEE PES Innovative Smart Grid Technologies—Asia (ISGT Asia), Tianjin, China, 21 May 2012–24 May 2012; pp. 1–2.
33. Bansal, R.C. *Handbook of Distributed Generation: Electric Power Technologies, Economics and Environmental Impacts*; Ramesh, B., Ed.; Springer: Cham, Switzerland, 2017; ISBN 9783319513430.
34. Xu, D.a.; Xu, D.; Blaabjerg, F.; Chen, W.; Zhu, N. *Modelling and Control of Doubly Fed Induction Generator Wind Power System under Non-Ideal Grid*, 1st ed.; Wiley-IEEE Press: Hoboken, NJ, USA, 2016; ISBN 978-1-119-17208-6.

35. Al-Quteimat, A. Control Layout of Doubly Fed Induction Generator with Respect to Low Voltage Ride through for Wind Energy Conversion System. 2018. Available online: <https://depositonce.tu-berlin.de/handle/11303/8209> (accessed on 1 February 2022). [[CrossRef](#)]
36. Xu, Z.; Rahman, M.F. Direct torque and flux regulation of an IPM synchronous motor drive using variable structure control approach. In Proceedings of the IECON 2004, 30th Annual Conference of the IEEE Industrial Electronics Society, Busan, South Korea, 2–6 November 2004; IEEE: Piscataway, NJ, USA, 2004; pp. 2487–2498.
37. Rahman, M.F.; Zhong, L.; Lim, K.W. A direct torque-controlled interior permanent magnet synchronous motor drive incorporating field weakening. *IEEE Trans. Ind. Appl.* **1998**, *34*, 1246–1253. [[CrossRef](#)]
38. Al-Quteimat, A.; Roccaforte, A.; Schafer, U. Performance improvement of direct torque control for doubly fed induction generator with 12 sector methodology. In Proceedings of the 2016 IEEE International Conference on Renewable Energy Research and Applications (ICRERA), Birmingham, UK, 20–23 November 2016; pp. 242–246. [[CrossRef](#)]